Biological and Medical Physics, Biomedical Engineering

Optical Coherence Tomography

Technology and Applications

von
Wolfgang Drexler, James G. Fujimoto

1. Auflage

Thematische Gliederung:

Augenheilkunde, Optometrie

Springer-Verlag Berlin Heidelberg 2013

Verlag C.H. Beck im Internet:
www.beck.de
ISBN 978 3 642 27643 9

Inhaltsverzeichnis: Optical Coherence Tomography – Drexler / Fujimoto

2

Theory of Optical Coherence Tomography

J.A. Izatt and M.A. Choma

2.1 Introduction

Several earlier publications have addressed the theory of optical coherence tomography (OCT) imaging. These include original articles [1–12], reviews [13, 14], and books/book chapters [15, 16]. Many of these publications were authored before the major revolution that Fourier domain techniques (here termed FDOCT) brought to OCT in the last few years, and thus were written primarily from the perspective of time-domain OCT (TDOCT). Also, relatively few prior publications have addressed lateral resolution in OCT systems, which, from an end-user perspective is of equal importance to the axial resolving power derived from low-coherence interferometry. The aim of this chapter is to present a unified theory of OCT, which includes a discussion of imaging performance in all three dimensions, and treats both Fourier and time domain OCT on equal footing as specializations of the same underlying principles.

A generic OCT system schematic is illustrated in Fig. 2.1. Light from a low-coherence source is directed into a 2 × 2 fiber–optic coupler implementing a simple Michelson interferometer. The coupler is assumed to split the incident optical power evenly into sample and reference arms, although many practical OCT system designs take advantage of unbalanced power splitting, as has been described theoretically and experimentally [8,9]. Light exiting the reference fiber is incident upon a reference delay and redirected back into the same fiber. Light exiting the sample fiber is incident upon a scanning mechanism designed to focus the beam on the sample and to scan the focused spot in one or two lateral directions, typically under computer control. Many specialized scanning systems have been developed for OCT imaging applications in microscopy, ophthalmoscopy, endoscopy, etc. The light backscattered or reflected from the sample is redirected back through the same optical scanning system into the sample arm fiber, where it is mixed with the returning reference arm light in the fiber coupler, and the combined light is made to interfere on the surface of a photoreceiver or detector. The electronic signals detected

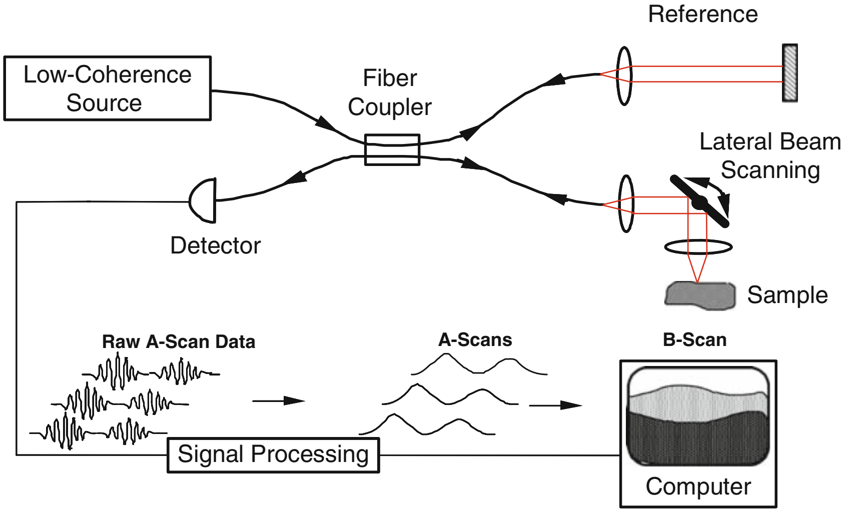

Fig. 2.1. Schematic of a generic fiber-optic OCT system. Bold lines represent fiber-optic paths, red lines represent free-space optical paths, and thin lines represent electronic signal paths

at the photoreceiver are processed into an A-scan, representing the depth-resolved reflectivity profile of the sample at the focal spot of the sample beam at a fixed lateral position of the scanning mechanism. As the scanning mechanism sweeps or steps the focused beam position across the sample, multiple A-scans are acquired and assembled in the computer into a two-dimensional cross-sectional image of the sample in the vicinity of the focal spot, termed as B-scan. Optionally, various alternative combinations of multi-dimensional lateral scanning and A-scan acquisition under computer control may be formed to create repeated A-scans at the same location as a function of time (termed M-scans), B-scans with lateral rather than depth priority, three-dimensional OCT volume datasets, and/or image improvement from OCT signal averaging in various combinations of dimensions.

In the case of TDOCT, the low-coherence source in Fig. 2.1 is broadband and continuous-wave (cw), the reference arm delay is repetitively scanned in length, a single-channel photoreceiver is employed, and the required signal processing consists of detecting the envelope of the detected fringe burst pattern corresponding to interference between the reference arm light and each successive scattering site in the sample. FDOCT systems are subdivided into spectral-domain (or spectrometer-based) systems referred to as SDOCT and swept-source systems termed SSOCT (alternatively called optical frequency-domain imaging or OFDI by some authors). In the case of SDOCT, the source is broadband and cw, the reference arm length is fixed at a position approximately corresponding to the position of the sample, and the spectral interference pattern between the light returning from the reference arm and all depths in the sample is dispersed by a spectrometer and collected simultaneously on an array detector such as a photodiode array or charge-coupled device (CCD). In the case of SSOCT, the source has narrow instantaneous linewidth but is rapidly swept in wavelength, and the spectral interference pattern is detected on a single or small number of photoreceivers as a function of time. The reference arm length is also fixed in SSOCT. In both SDOCT and SSOCT forms of FDOCT, the spectral interference pattern encodes in its spectral frequency content the entire depth-resolved structure of the sample at the position of the focal spot, and the A-scan may be recovered as described below, using an inverse Fourier transform. Additional signal processing steps (such as interpolation) may also be required in FDOCT to prepare the spectral interferogram for the inverse Fourier transform, so that the data is linearly sampled in wavenumber, addition of phase terms to correct for dispersion mis-matches between the sample and reference arms, and others.

2.2 Confocal Gating and Lateral Resolution in OCT Systems

Some previous analyses have described the lateral resolution and axial field of view of OCT systems as illustrated in Fig. 2.1 as the spot size and depth of focus of an assumed Gaussian profile sample arm beam in the region of the beam focus. This approach is a reasonable approximation and provides useful insight into the trade-off between these quantities, specifically that spot size is proportional to the numerical aperture (NA) of the sample arm focusing optics, while depth of focus is proportional to NA^2. However, it is more correct to treat the sample arm of an OCT system as a reflection-mode scanning confocal microscope, in which the singlemode optical fiber serves as a pinhole aperture for both illumination and collection of light from the sample. Even for OCT systems that do not employ fiber optics, the antenna response function of the homodyne wave mixing inherent to OCT can be shown to be equivalent to confocality. Confocal microscopes using fiber optic delivery and detection have been well described in the literature, including their lateral and axial point-spread function behavior for single and multimode fiber operation [17–19]. For singlemode optical fibers such as those used in OCT, the expressions for both lateral- and axial-detected intensity reduce to those for an ideal confocal microscope with a diminishingly small pinhole aperture. Confocal microscopes have the advantage of slightly improved lateral resolution over conventional bright-field microscopes and the ability to perform "optical sectioning" due to their peaked axial response (unlike conventional brightfield microscopes, for which out-of-focus light is blurred, but not attenuated). A summary of results characterizing these quantities in lateral and axial directions are presented in Fig. 2.2. The optical system is assumed to be cylindrically symmetric, and so only one lateral dimension is described.

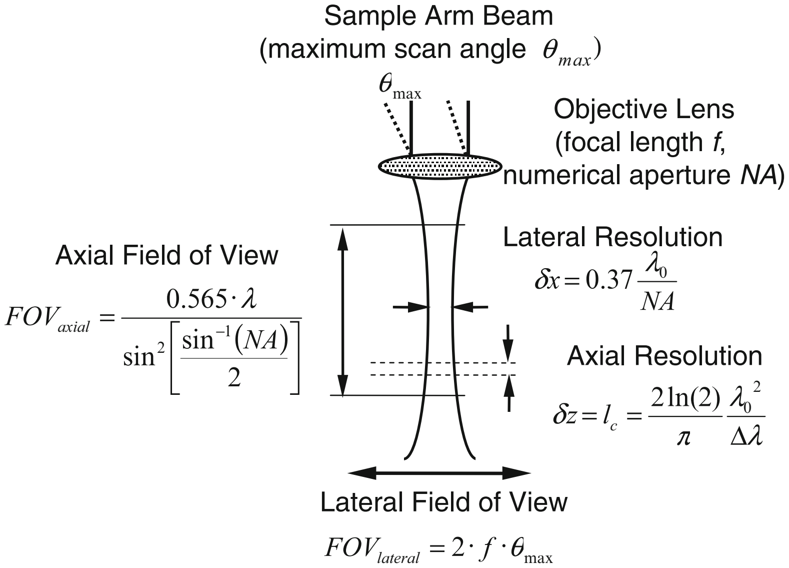

Fig. 2.2. Schematic of generic OCT sample arm optics. Formulas are provided for axial field of view $\mathrm{FOV}_{\mathrm{axial}}$ and lateral resolution δx (assuming these quantities are dominated by the confocal geometrical optics), axial resolution δz (assuming it is limited by the low-coherence interferometer), and for lateral field of view $\mathrm{FOV}_{\mathrm{lateral}}$ (assuming a simple f-theta scanning system)

An expression for the detected intensity from a point reflector placed in the focal plane of an ideal reflection confocal microscope as a function of lateral position is given by

$$I(v) = \left(\frac{2J_1(v)}{v}\right)^4, \tag{2.1}$$

where $J_1(v)$ is a first-order Bessel function of the first kind and v is the normalized lateral range parameter defined by $v = 2\pi x \sin(\alpha)/\lambda_0$. Here, x is the lateral distance from the optical axis, α is half the angular optical aperture subtended by the objective, and λ_0 is the center wavelength of the light source. Note that the numerical aperture of the objective is given by $\mathrm{NA} = \sin(\alpha)$, assuming it is properly filled. We interpret (2.1) as the lateral point-spread function of an OCT system at the position of its focal plane, and characterize it by defining the lateral resolution δx as its full width at half maximum power, which calculates to

$$\delta x = 0.37\frac{\lambda_0}{\sin(\alpha)} = 0.37\frac{\lambda_0}{\mathrm{NA}}. \tag{2.2}$$

The lateral field of view for an OCT system depends greatly upon the details of the lateral scanning system employed. A particularly simple scanning system employs some means to rotate the sample arm beam through the input aperture of the objective lens to a maximum one-sided scan angle $\theta_{\max}$. In this case, the lateral field of view of the OCT system is simply given by $\mathrm{FOV}_{\mathrm{lateral}} = 2f\theta_{\max}$.

We follow the convention in confocal microscopy [17, 18] and describe the axial response of the OCT sample arm optics as the confocal response to a planar rather than point reflector. The detected intensity of an ideal confocal microscope from a planar reflector as a function of the reflector position along the optic axis is given by

$$I(u) = \left(\frac{\sin(u/2)}{(u/2)}\right)^2, \tag{2.3}$$

where u is the normalized axial range parameter defined by $u = 8\pi z \sin^2(\alpha/2)/\lambda_0$. The axially peaked response of a confocal microscope gives it its well-known depth sectioning capability. This is also the response we would expect by translating a mirror axially through the focus of an OCT sample arm. If the length of this function is comparable to the axial response of the OCT system arising from low-coherence interferometry (as described below), then the overall axial response of the OCT system should properly be described as the convolution of these two functions. OCT systems operating in this regime have been referred to as optical coherence microscopy or OCM systems [2, 20, 21]. In OCM, however, considerable effort must be expended to align the “confocal” and “coherence” gates, and to keep them aligned as depth scanning is performed. In most OCT applications designed for practical clinical and research applications, a relatively low numerical aperture objective is used so that the lateral resolution δx is approximately matched to the axial resolution δz defined by the low-coherence interferometer (see (2.8) below), and thus approximately isotropic resolution imaging is performed. Under this condition, the confocal gate length is much larger than the lateral resolution since it scales as the square of the numerical aperture. However, the confocal gate length still limits the axial range over which the low-coherence interferometric depth scanning may usefully operate. We define the full width at half maximum power of the confocal axial response function as the axial field-of-view $\mathrm{FOV}_{\mathrm{axial}}$ of the OCT system, which calculates to

$$\mathrm{FOV}_{\mathrm{axial}} = \frac{0.565\lambda}{\sin^2[\alpha/2]} = \frac{0.565\lambda}{\sin^2\left[\frac{\sin^{-1}(\mathrm{NA})}{2}\right]}. \tag{2.4}$$

2.3 Axial Ranging with Low-Coherence Interferometry

The fundamental quality that differentiates optical coherence tomography (OCT) from other forms of optical microscopy is that the predominant axial component of image formation derives from a ranging measurement performed using low-coherence interferometry. Consider the Michelson interferometer

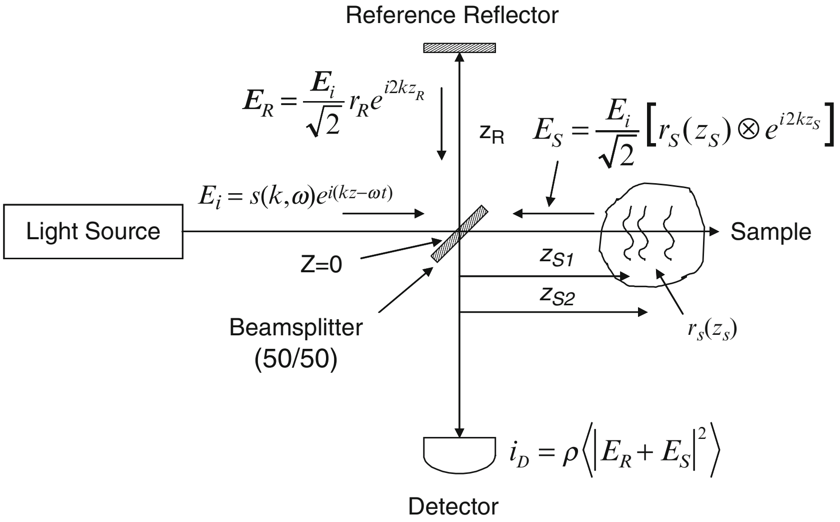

Fig. 2.3. Schematic of a Michelson interferometer used in OCT

illustrated in Fig. 2.3. The interferometer is illuminated by a polychromatic plane wave whose electric field expressed in complex form is $E_\mathrm{i} = s(k,\omega)\,\mathrm{e}^{\mathrm{i}(kz-\omega t)}$. Here, $s(k,\omega)$ is the electric field amplitude as a function of the wavenumber $k = 2\pi/\lambda$ and angular frequency $\omega = 2\pi\nu$, which are respectively the spatial and temporal frequencies of each spectral component of the field having wavelength λ. The wavelength λ and frequency ν are coupled by the index of refraction $n(\lambda)$ (which is wavelength-dependent in dispersive media) and vacuum speed of light c according to $c/n(\lambda) = \lambda\nu$. The beamsplitter is assumed to have an achromatic (wavelength-independent) power splitting ratio of 0.5. The reference reflector is assumed to have electric field reflectivity r_R and power reflectivity $R_\mathrm{R} = |r_\mathrm{R}|^2$. The distance from the beamsplitter to the reference reflector is z_R.

The sample under interrogation is characterized by its depth-dependent electric field reflectivity profile along the sample beam axis $r_\mathrm{S}(z_\mathrm{S})$, where z_S is the pathlength variable in the sample arm measured from the beamsplitter. In general $r_\mathrm{S}\ (z_\mathrm{S})$ is continuous, resulting from the continuously varying refractive index of biological tissues and other samples. It may also be complex, encoding the phase as well as the amplitude of each reflection. However, for an illustrative example, we assume a series of N discrete, real delta-function reflections of the form $r_\mathrm{S}(z_\mathrm{S}) = \sum\limits_{n=1}^{N} r_{\mathrm{S}n}\delta(z_\mathrm{S} - z_{\mathrm{S}n})$, each reflection characterized by its electric field reflectivity $r_{\mathrm{S}1},\ r_{\mathrm{S}2}\ldots$, and pathlength from the beamsplitter of $z_{\mathrm{S}1},\ z_{\mathrm{S}2}\ldots$ (see Fig. 2.4). The power reflectivity of each reflector is given by the magnitude squared of the electric field reflectivity, for example $R_{\mathrm{S}1} = |r_{\mathrm{S}1}|^2$. *The reconstruction of the function* $\sqrt{R_\mathrm{S}(z_\mathrm{S})}$ *from*

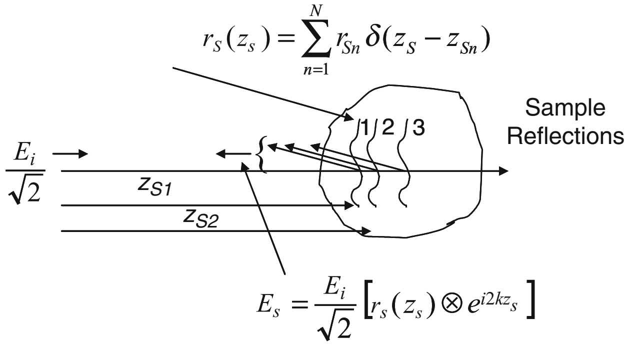

Fig. 2.4. Exemplary model for a sample comprising a series of discrete reflectors

noninvasive interferometric measurements is the goal of low-coherence interferometry in OCT. The electric field passing through the beamsplitter after returning from the sample arm is $E_\mathrm{s} = \frac{E_\mathrm{i}}{\sqrt{2}}\left[r_\mathrm{S}(z_\mathrm{S}) \otimes \mathrm{e}^{\mathrm{i}2kz_\mathrm{S}}\right]$, where $\otimes$ represents convolution, and the factor of 2 in the exponential kernel accounts for the round-trip pathlength to each sample reflection. Note that for most samples such as biological tissues imaged with OCT, sample reflectivities $R_{\mathrm{S}1}$, $R_{\mathrm{S}2} \ldots$ are typically very small (on the order of $\sim 10^{-4}$ to 10^{-5}); thus the returned reference field typically dominates the reflected sample field. Indeed, published studies have shown that selection of the appropriate reference reflectivity is an important design criterion in OCT system design [8,9].

For the example of discrete reflectors, the fields incident on the beamsplitter after returning from the reference and sample arms are given by $E_\mathrm{R} = \frac{E_\mathrm{i}}{\sqrt{2}} r_\mathrm{R}\,\mathrm{e}^{\mathrm{i}2kz_\mathrm{R}}$ and $E_\mathrm{s} = \frac{E_\mathrm{i}}{\sqrt{2}} \sum_{n=1}^{N} r_{\mathrm{S}n}\,\mathrm{e}^{\mathrm{i}2kz_{\mathrm{S}n}}$, respectively. The returning fields are halved in power upon passing through the beamsplitter again and interfere at the square-law detector, which generates a photocurrent proportional to the square of the sum of the fields incident upon it, given by $I_\mathrm{D}(k,\omega) = \frac{\rho}{2}\left\langle |E_\mathrm{R} + E_\mathrm{S}|^2 \right\rangle = \frac{\rho}{2}\left\langle (E_\mathrm{R} + E_\mathrm{S})(E_\mathrm{R} + E_\mathrm{S})^* \right\rangle$. Here, ρ is the responsivity of the detector (units Amperes/Watt), the factor of 2 reflects the second pass of each field through the beamsplitter, and the angular brackets denote integration over the response time of the detector. Arbitrarily setting $z = 0$ at the surface of the beamsplitter, and expanding for the detector current gives

$$I_\mathrm{D}(k,\omega) = \frac{\rho}{2}\left\langle \left| \frac{s(k,\omega)}{\sqrt{2}} r_\mathrm{R}\,\mathrm{e}^{\mathrm{i}(2kz_\mathrm{R} - \omega t)} + \frac{s(k,\omega)}{\sqrt{2}} \sum_{n=1}^{N} r_{\mathrm{S}n}\,\mathrm{e}^{\mathrm{i}(2kz_{\mathrm{S}n} - \omega t)} \right|^2 \right\rangle . \tag{2.5}$$

Expanding the magnitude squared functions in (2.5) eliminates the terms dependent upon the temporal angular frequency $\omega = 2\pi\nu$, which is reasonable since ν oscillates much faster than the response time of any practical detector.

This leaves the temporally invariant terms

$$\begin{aligned} I_{\mathrm{D}}(k) = & \frac{\rho}{4}[S(k)(R_{\mathrm{R}} + R_{\mathrm{S1}} + R_{\mathrm{S2}} + \ldots)] \\ & + \frac{\rho}{4}\left[S(k)\sum_{n=1}^{N}\sqrt{R_{\mathrm{R}}R_{\mathrm{S}n}}\left(\mathrm{e}^{\mathrm{i}2k(z_{\mathrm{R}}-z_{\mathrm{S}n})} + \mathrm{e}^{-\mathrm{i}2k(z_{\mathrm{R}}-z_{\mathrm{S}n})}\right)\right] \\ & + \frac{\rho}{4}\left[S(k)\sum_{n\neq m=1}^{N}\sqrt{R_{\mathrm{S}n}R_{\mathrm{S}m}}\left(\mathrm{e}^{\mathrm{i}2k(z_{\mathrm{S}n}-z_{\mathrm{S}m})} + \mathrm{e}^{-\mathrm{i}2k(z_{\mathrm{S}n}-z_{\mathrm{S}m})}\right)\right]. \end{aligned} \tag{2.6}$$

Here, $S(k) = \langle |s(k,\omega|^2\rangle$ is substituted, which encodes the power spectral dependence of the light source. As an illustrative example, a Gaussian-shaped light source spectrum is convenient to use in modeling OCT because it approximates the shape of actual light sources and also has useful Fourier transform properties. The normalized Gaussian function $S(k)$ and its inverse Fourier transform $\gamma(z)$ are given by

$$\gamma(z) = \mathrm{e}^{-z^2\Delta k^2} \overset{F}{\longleftrightarrow} S(k) = \frac{1}{\Delta k\sqrt{\pi}}\,\mathrm{e}^{-\left[\frac{(k-k_0)}{\Delta k}\right]^2} \tag{2.7}$$

and are illustrated in Fig. 2.5. Here, k_0 represents the central wavenumber of the light source spectrum and Δk represents its spectral bandwidth, corresponding to the half-width of the spectrum at $1/e$ of its maximum. As will be seen below, the inverse Fourier transform of the source spectrum $\gamma(z)$, otherwise called the "coherence function," dominates the axial point-spread function (PSF) in OCT imaging systems (at least those employing a low numerical aperture focusing objective, as pointed out in Sect. 2.2). The PSF is commonly characterized by its full width at half the maximum (FWHM) value, and is the definition of the round-trip "coherence length" of the light

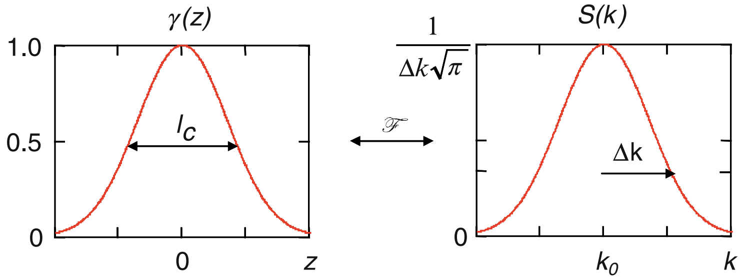

Fig. 2.5. Illustration of Fourier transform relationship between the Gaussian-shaped coherence function $\gamma(z)$ (characterized by the coherence length l_{c}), and the light source spectrum $S(k)$ (characterized by the central wavenumber k_0 and wavenumber bandwidth Δk)

source l_c. The coherence length is an explicit function of the light source bandwidth, stated both in wavenumber and wavelength terms as

$$l_\mathrm{c} = \frac{2\sqrt{\ln(2)}}{\Delta k} = \frac{2\ln(2)}{\pi}\frac{\lambda_0^2}{\Delta\lambda}. \tag{2.8}$$

Here, $\lambda_0 = 2\pi/k_0$ is the center wavelength of the light source and $\Delta\lambda$ is its wavelength bandwidth, defined as the FWHM of its wavelength spectrum (so that $\Delta k = \frac{\pi}{\sqrt{\ln(2)}}\frac{\Delta\lambda}{{\lambda_0}^2}$). Note the inverse relationship between the coherence length and the light source bandwidth.

Using Euler's rule to simplify (2.6) generates a real result for the detector current as a function of wavenumber, commonly known as the "spectral interferogram"

$$\begin{aligned} I_\mathrm{D}(k) = {} & \frac{\rho}{4}\left[S(k)\left[R_\mathrm{R} + R_\mathrm{S1} + R_\mathrm{S2} + \ldots\right]\right] \quad \text{“DC Terms”} \\ & + \frac{\rho}{2}\left[S(k)\sum_{n=1}^{N}\sqrt{R_\mathrm{R}R_{\mathrm{S}n}}\left(\cos\left[2k(z_\mathrm{R} - z_{\mathrm{S}n})\right]\right)\right] \quad \text{“Cross-correlation Terms”} \\ & + \frac{\rho}{4}\left[S(k)\sum_{n\neq m=1}^{N}\sqrt{R_{\mathrm{S}n}R_{\mathrm{S}m}}\cos\left[2k(z_{\mathrm{S}n} - z_{\mathrm{S}m})\right]\right] \quad \text{“Auto-correlation Terms”}. \end{aligned} \tag{2.9}$$

The result in (2.5) includes three distinct components:

1. A pathlength-independent offset to the detector current, scaled by the light source wavenumber spectrum and with amplitude proportional to the power reflectivity of the reference mirror plus the sum of the sample reflectivities. This term is often referred to as "constant" or "DC" component. This is the largest component of the detector current if the reference reflectivity dominates the sample reflectivity.
2. A "cross-correlation" component for each sample reflector, which depends upon both light source wavenumber and the pathlength difference between the reference arm and sample reflectors. This is the desired component for OCT imaging. Since these components are proportional to the square root of the sample reflectivities, they are typically smaller than the DC component. However, the square root dependence represents an important logarithmic gain factor over direct detection of sample reflections.
3. "Autocorrelation" terms representing interference occurring between the different sample reflectors appear as artifacts in typical OCT system designs (exceptions occur in common-path system designs, in which the autocorrelation component represents the desired signal). Since the autocorrelation terms depend linearly upon the power reflectivity of the sample reflections, a primary tool for decreasing autocorrelation artifacts is selection of the proper reference reflectivity so that the autocorrelation terms are small compared to the DC and interferometric terms.

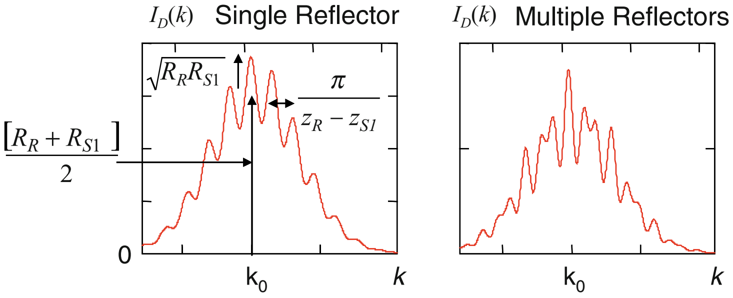

Fig. 2.6. Important features of the spectral interferogram. For a single sample reflector of field reflectivity $r_{S1} = 0.1$ (*left*) the cross-correlation component with amplitude $\sqrt{R_R R_{S1}}$ and wavenumber period $\pi/(z_R - z_{S1})$ rides on top of the DC term of amplitude $[R_R + R_{S1}]/2$ (factors of $\rho S(k)$ are left out for clarity). For multiple reflectors, the cross-correlation component is a superposition of cosinusoids

It is useful to gain an intuitive understanding of the form of (2.9), as well as the effect that different source spectra and different numbers of sample reflectors and their distributions have upon it. For a single reflector, only DC and a single interferometric term are present, and the source spectrum is modulated by a simple cosinusoid whose period is proportional to the distance between the sample and reference reflectors, as illustrated in Fig. 2.6. In addition, the amplitude of spectral modulation or "visibility" of the spectral fringes is proportional to the amplitude reflectivity of the sample reflector $\sqrt{R_{S1}}$. For the case of multiple reflectors, the spectrum is modulated by multiple cosinusoids, each having a frequency and amplitude characteristic of the sample reflection which gives rise to it. In addition, if more than one reflector is present in the sample, autocorrelation components modulated according to the pathlength difference between the sample reflectors and proportional to the product of their amplitude reflectivities also appear. Since the sample amplitude reflectivities are typically small, these terms are typically small, and also since reflections in the sample tend to be clumped closely together compared to the distance between the sample and the reference reflector, their modulation frequencies tend to be small.

2.4 Fourier Domain Low Coherence Interferometry

In Fourier domain OCT (FDOCT), the wavenumber-dependent detector current $I_D(k)$ in (2.9) is captured and processed using Fourier analysis to reconstruct an approximation of the internal sample reflectivity profile $\sqrt{R_S(z_S)}$. The process for capturing $I_D(k)$ depends upon the experimental details of the detection apparatus. In spectral domain OCT (SDOCT, also called spectrometer-based OCT), a broadband light source is used, and all spectral components of $I_D(k)$ are captured simultaneously on a detector array placed at the output of a spectrometer [22–24]. In swept-source OCT (SSOCT, also called optical frequency-domain imaging or OFDI), the spectral components of $I_{\mathrm{D}}(k)$ are captured sequentially by recording the signal in a single detector while synchronously sweeping the wavenumber of a narrowband swept-laser source [25–28].

The sample reflectivity profile $r_{\mathrm{S}}(z_{\mathrm{S}})$ is estimated from the inverse Fourier transform of $I_{\mathrm{D}}(k)$. Making use of the Fourier transform pair $\frac{1}{2}\left[\delta(z+z_0) + \delta(z-z_0)\right] \xleftrightarrow{F} \cos kz_0$ and the convolution property of Fourier transforms $x(z) \otimes y(z) \xleftrightarrow{F} X(k)Y(k)$, the inverse Fourier transform of (2.9) may be calculated as

$$\begin{aligned} i_{\mathrm{D}}(z) = {} & \frac{\rho}{8}\left[\gamma(z)\left[R_{\mathrm{R}} + R_{\mathrm{S1}} + R_{\mathrm{S2}} + \ldots\right]\right] \text{ “DC Terms”} \\ & + \frac{\rho}{4}\left[\gamma(z) \otimes \sum_{n=1}^{N} \sqrt{R_{\mathrm{R}} R_{\mathrm{S}n}}\,\left(\delta(z \pm 2(z_{\mathrm{R}} - z_{\mathrm{S}n}))\right)\right] \\ & \text{“Cross-correlation Terms”} \\ & + \frac{\rho}{8}\left[\gamma(z) \otimes \sum_{n \neq m=1}^{N} \sqrt{R_{\mathrm{S}n} R_{\mathrm{S}m}}\,\left(\delta(z \pm 2(z_{\mathrm{S}n} - z_{\mathrm{S}m}))\right)\right] \\ & \text{“Auto-correlation Terms”.} \end{aligned} \tag{2.10}$$

Note that the desired sample field reflectivity profile $\sqrt{R_{\mathrm{S}}(z_{\mathrm{S}})} = \sum_{n=1}^{N} \sqrt{R_{\mathrm{S}n}}\,\delta(z_{\mathrm{S}} - z_{\mathrm{S}n})$ is indeed embedded within the cross-correlation terms of (2.10), although it is surrounded by several confounding factors. Carrying out the convolutions by taking advantage of the sifting property of the delta function, we obtain the result of the interferometric measurement, referred to as the “A-scan”:

$$\begin{aligned} i_{\mathrm{D}}(z) = {} & \frac{\rho}{8}\left[\gamma(z)\left[R_{\mathrm{R}} + R_{\mathrm{S1}} + R_{\mathrm{S2}} + \ldots\right]\right] \\ & + \frac{\rho}{4}\sum_{n=1}^{N} \sqrt{R_{\mathrm{R}} R_{\mathrm{S}n}}\,\left[\gamma[2(z_{\mathrm{R}} - z_{\mathrm{S}n})] + \gamma[-2(z_{\mathrm{R}} - z_{\mathrm{S}n})]\right] \\ & + \frac{\rho}{8}\sum_{n \neq m=1}^{N} \sqrt{R_{\mathrm{S}n} R_{\mathrm{S}m}}\,\left[\gamma[2(z_{\mathrm{S}n} - z_{\mathrm{S}m})] + \gamma[-2(z_{\mathrm{S}n} - z_{\mathrm{S}m})]\right]. \end{aligned} \tag{2.11}$$

The results in (2.10) and (2.11) for the example of discrete sample reflectors and a Gaussian-shaped source spectrum are plotted in Fig. 2.7. As can be seen in the figure, the sample field reflectivity profile $\sqrt{R_{\mathrm{S}}(z_{\mathrm{S}})} = \sum_{n=1}^{N} \sqrt{R_{\mathrm{S}n}}\,\delta(z_{\mathrm{S}} - z_{\mathrm{S}n})$ is reproduced in the cross-correlation terms with the following modifications. First, the zero position of the reflectivity profile appears at the position of the reference reflector z_{R}, rather than the position of the

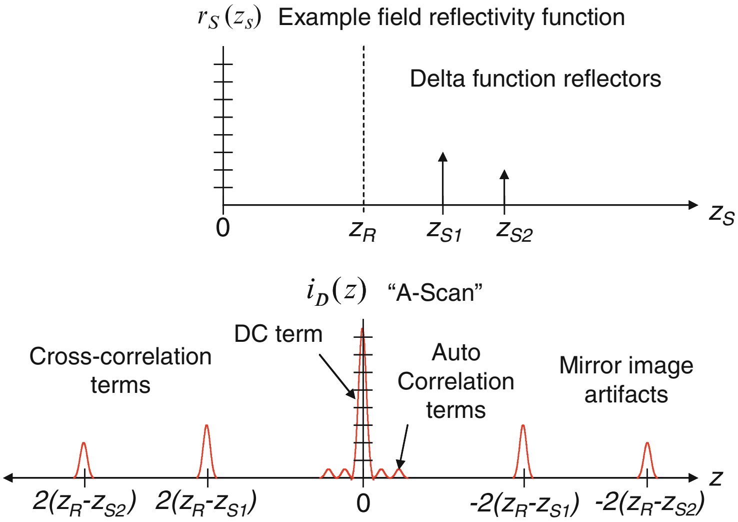

Fig. 2.7. Illustration of the example discrete-reflector sample field reflectivity function $r_\mathrm{S}(z_\mathrm{S}) = \sum_{n=1}^{N} r_{\mathrm{S}n}\delta(z_\mathrm{S} - z_{\mathrm{S}n})$ (*top*), and the A-scan resulting from Fourier-domain low-coherence interferometry

beamsplitter. Second, the apparent displacement of each sample reflector from the reference position is doubled (which can be understood from the fact that the interferometer measures the round-trip distance to each reflector). We accommodate this by defining a new single-pass depth variable $\widehat{z} = 2z$. Third, each reflector appears broadened or blurred out to a width of about a coherence length by convolution with the function $\gamma(z)$. This is precisely the definition of an imaging system PSF. Given the inverse relationship of the coherence length to the light source bandwidth, the clearest path to increase the fidelity of the estimate of $\sqrt{R_\mathrm{S}(z_\mathrm{S})}$ is to use as broad bandwidth sources as possible. Fourth, the magnitude of the detected sample reflectivity, which can be very small, is amplified by the large homodyne gain factor represented by the strong reference reflectivity $\sqrt{R_\mathrm{R}}$. All the modifications listed so far can be dealt with through proper interpretation of the data, i.e., realization that the zero position corresponds to the position of the reference reflector, relabeling axial distances to account for the factor of 2, and accounting for the homodyne gain factor.

A number of additional modifications to the field reflectivity profile are termed artifacts and are more serious. First, as seen in the cross-correlation terms in (2.10) and (2.11), a mirror image of the blurred version of $\sqrt{R_\mathrm{S}(z_\mathrm{S})}$ appears on the opposite side of zero pathlength, i.e., the reference reflector position. This is termed the complex conjugate artifact in FDOCT, and is simply understood from the fact that since the detected interferometric spectrum is necessarily real, its inverse Fourier transform must be Hermitian symmetric, i.e., its positive and negative distances are complex conjugates of each other and therefore if they are real, they must be identical. This artifact is not serious so long as the sample can be kept entirely to one side of zero path length, in which case it can be dealt with by simply displaying only the positive or negative distances. However, if the sample strays over the zero pathlength border, it begins to overlap its mirror image, an effect that cannot be removed by image processing alone. A number of approaches are under development for removing this complex conjugate artifact ([29–36], see also Sect. 2.6.2).

Additional image artifacts also arise from the DC and auto-correlation terms in (2.10) and (2.11). The DC terms give rise to a large artifactual signal centered at zero pathlength difference. The FWHM value of the DC artifact is only one coherence length wide; however, the signal amplitude is so much larger than the desired cross-correlation terms that the wings of the Gaussian-shaped PSF from (2.7) can overwhelm desired signal components much farther away. Since the largest component of the DC artifact comes from the reference reflector (with reflectivity near 1), a simple method to eliminate that component is to record the amplitude of the spectral interferometric signal (2.9) with the reference reflector but no sample present, then to subtract this signal component from each subsequent spectral interferometric signal acquired. The autocorrelation terms in (2.10) and (2.11) also give rise to artificial signals at and near the zero pathlength position, since the distance between reflectors in a sample is typically much smaller than the distance between the sample reflectors and the reference arm path length. The best method to eliminate the autocorrelation signals is to ensure that the reference reflectivity is sufficient so that the amplitude of the autocorrelation terms is very small compared to the cross-correlation terms.

2.5 Time Domain Low Coherence Interferometry

In traditional or time-domain OCT (TDOCT), the wavenumber-dependent detector current $I_{\mathrm{D}}(k)$ in (2.9) is captured on a single receiver while the reference delay z_{r} is scanned to reconstruct an approximation of the internal sample reflectivity profile $\sqrt{R_{\mathrm{S}}(z_{\mathrm{S}})}$. The result is obtained by the integration of (2.9) over all k:

$$\begin{aligned} I_{\mathrm{D}}(z_{\mathrm{R}}) = {} & \frac{\rho}{4}\left[S_0\left[R_{\mathrm{R}} + R_{\mathrm{S1}} + R_{\mathrm{S2}} + \ldots\right]\right] \text{ “DC Offset”} \\ & + \frac{\rho}{2}\left[S_0 \sum_{n=1}^{N} \sqrt{R_{\mathrm{R}} R_{\mathrm{S}n}}\, \mathrm{e}^{-(z_{\mathrm{R}}-z_{\mathrm{S}n})^2 \Delta k^2} \cos\left[2k_0(z_{\mathrm{R}} - z_{\mathrm{S}n})\right]\right] \qquad (2.12) \\ & \text{“Fringe Bursts”.} \end{aligned}$$

Here, $S_0 = \int\limits_0^\infty S(k)\,\mathrm{d}k$ is the spectrally integrated power emitted by the light source. The resulting time-domain “A-scan” resulting from such a measurement is illustrated in Fig. 2.8. Note that the sample reflectivity profile

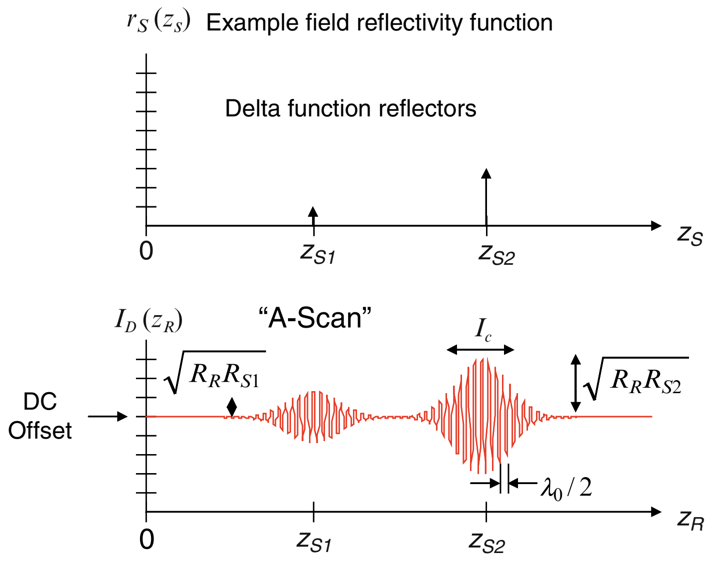

Fig. 2.8. Illustration of the example discrete-reflector sample field reflectivity function $r_\mathrm{S}(z_\mathrm{S}) = \sum_{n=1}^{N} r_{\mathrm{S}n}\delta(z_\mathrm{S} - z_{\mathrm{S}n})$ (*top*), and the A-scan resulting from time-domain low-coherence interferometry

convolved with the source coherence function is again recapitulated in the result, resident on a DC offset proportional to the sum of the reference and sample power reflectivities. In addition, the convolved sample reflectivity profile is modulated by a cosinusoidal carrier wave modulation at a frequency proportional to the source center wavenumber k_0 and the difference between reference and sample arm lengths $z_\mathrm{R} - z_{\mathrm{S}n}$. Since the reference arm length z_R is typically scanned as a function of time in TDOCT systems, this carrier provides a convenient modulation frequency for lock-in detection, which provides for high sensitivity detection of the reflectivity envelope and rejection of the DC offset.

2.6 Practical Aspects of FDOCT Signal Processing

2.6.1 Sensitivity Falloff and Sampling Effects in FDOCT

While the FDOCT spectral interferogram of (2.9) and its continuous-time inverse Fourier transform (2.11) illustrate the fundamental principle underlying spectrometer-based (SD) and swept-source (SS) OCT, in practical implementations of these devices, several additional factors must be taken into account. The spectral interferogram data is generated by instrumentation having real-world limitations, and is typically acquired by a sampling

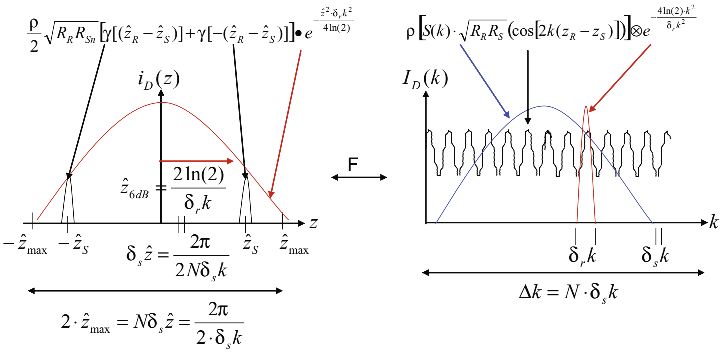

Fig. 2.9. Conceptual basis for sensitivity falloff and maximum imaging depth in FDOCT. Note that the depth-dependent falloff in sensitivity is directly related to the resolution of the interference spectrum, which is dominated by the source linewidth in SSOCT and the spectrometer resolution in FDOCT

operation for rapid digital signal computation of its inverse Fourier transform. Figure 2.9 illustrates conceptually the effects of finite spectral resolution and sampling upon the spectral interferogram and its inverse Fourier transform.

First, the instrumentation for acquiring the spectral interferogram always has limited spectral resolution, here denoted by $\delta_\mathrm{r}k$. In SSOCT, $\delta_\mathrm{r}k$ is limited by the instantaneous lineshape of the swept laser source, while in SDOCT, $\delta_\mathrm{r}k$ is the spectral resolution of the spectrometer (including the finite spacing of the CCD pixels, whose effect on resolution in SDOCT has also been modeled explicitly [10, 37]). We model the effect of finite spectral resolution by convolving the ideal spectral interferogram from (2.9) with a Gaussian function having half-maximum width $\delta_\mathrm{r}k$, which we interpret as the FWHM spectral resolution. Via the convolution property, the A-scan data is thus multiplied by a sensitivity "falloff" factor whose shape is given by the inverse Fourier transform of the Gaussian-shaped resolution factor, which is also a Gaussian:

$$i_\mathrm{D}(\hat{z})\bullet\exp\left[-\frac{\hat{z}^2\delta_\mathrm{r}k^2}{4\ln(2)}\right]\xleftrightarrow{F} I_\mathrm{D}(k)\otimes\exp\left[-\frac{4\ln(2)k^2}{\delta_\mathrm{r}k^2}\right]. \tag{2.13}$$

Use here of the re-scaled depth variable $\hat{z}=2z$ removes the apparent depth-doubling factor in FDOCT and allows processed A-scan data to be compared directly to sample structure. The exponential falloff of sensitivity with depth can be understood as the decreasing visibility of higher fringe frequencies corresponding to large sample depths. It may be characterized by defining the one-sided depth at which the sensitivity falls off by a factor of $1/2$ or 6 dB in optical SNR units:

$$\hat{z}_{6\,\mathrm{dB}}=\frac{2\ln(2)}{\delta_\mathrm{r}k}=\frac{\ln(2)}{\pi}\frac{\lambda_0^2}{\delta_\mathrm{r}\lambda}. \tag{2.14}$$

Here $\hat{z}_{6\,\mathrm{dB}}$ is given in terms of the FWHM spectral resolution in both wavenumber ($\delta_{\mathrm{r}}k$) and wavelength ($\delta_{\mathrm{r}}\lambda$) terms, the latter of which is recognizable as one-half of the coherence length corresponding to the spectral resolution.

The second major consideration in real-world processing of FDOCT data is that computer-based detection involves sampling the spectral interferogram. We assume the interferogram is sampled with spectral sampling interval $\delta_{\mathrm{s}}k$ into M spectral channels linearly spaced in k. The total wavenumber range collected is thus $\Delta k = M\delta_{\mathrm{s}}k$, and this in turn sets the sampling interval in the z-domain $\delta_{\mathrm{s}}\hat{z} = 2\pi/(2\Delta k)$, where the extra factor of 2 in the denominator arises from use of the rescaled depth parameter $\hat{z}$. The maximum and minimum depth samples are thus given by the Nyquist criterion as

$$\pm z_{\max} = \pm\frac{\pi}{2\cdot\delta_{\mathrm{s}}k} = \pm\frac{\lambda_0^2}{4\cdot\delta_{\mathrm{s}}\lambda}. \tag{2.15}$$

A summary of the results of this section is provided in Table 2.1. In addition to these limitations imposed by spectral resolution and sampling which are difficult to overcome, additional real-world complications arise, which can be handled with appropriate digital signal processing. First, the spectral interferogram data may not be acquired as a linear function of optical wavenumber, which is the required conjugate variable for imaging depth in the inverse Fourier transform operation underlying FDOCT. For example, grating-based spectrometers typically disperse spectra approximately linearly in wavelength rather than wavenumber, and swept-wavelength laser sources may be subject to any number of nonlinearities. For each of these cases, solutions involving clever spectrometer designs, clever k-triggering schemes, or as a last resort digital spectral resampling after acquisition have all been described. In addition, dispersion effects due to mis-matched glass or tissue lengths in the sample and reference arms may also be corrected by the addition

Table 2.1. Effects of sampling and finite spectral resolution in Fourier-Domain OCT (FDOCT) systems

	Maximum one-sided imaging depth $\widehat{z}_{\max}$	6dB SNR falloff point $\widehat{z}_{6dB}$
Wavenumber units ($k = 2\pi/\lambda$)	$\frac{\pi}{2\cdot\delta_{\mathrm{s}}k}$	$\frac{2\ln(2)}{\delta_{\mathrm{r}}k}$
Wavelength units	$\frac{\lambda_0^2}{4\cdot\delta_{\mathrm{s}}\lambda}$	$\frac{\ln(2)}{\pi}\frac{\lambda_0^2}{\delta_{\mathrm{r}}\lambda}$

δ_{s} and δ_{r} represent the spectral sampling interval and FWHM spectral resolution, respectively. The maximum imaging depth $z_{\max}$ may be doubled by the use of methods for removing the complex conjugate ambiguity artifact of appropriate phase factors to the spectral interferometric data prior to inverse Fourier transformation.

2.6.2 Artifact Removal in FDOCT by Phase Shifting

The DC, autocorrelation, and complex conjugate artifacts in FDOCT may in principle be removed by utilizing principles and techniques borrowed from phase-shift interferometry [30, 31, 38, 39]. If the interferometer is modified to provide for the introduction of a variable single-pass phase delay ϕ (round-trip phase delay 2ϕ) between the reference and sample arms, then a set of spectral interferograms may be acquired with different phase delays, which can be combined in signal processing to eliminate the undesired artifacts. For example, Fig. 2.10 illustrates an FDOCT interferometer with a variable phase modulator placed in the reference arm, such that the reference field returning from the reference arm is modified to $E_{\mathrm{R}} = \frac{E_{\mathrm{i}}}{\sqrt{2}} r_{\mathrm{R}}\, \mathrm{e}^{\mathrm{i}(2kz_{\mathrm{R}}+2\phi)}$. There are a number of approaches for introducing such phase delays. Phase modulators based on electro-optic, acousto-optic, and photoelastic modulators may be utilized, or the reference mirror itself may be dithered by mounting it on a piezoelectric transducer. Such transducers have the advantage of relative simplicity; however, their use requires that phase-shifted spectral interferograms be acquired sequentially; thus the resulting artifact reduction occurs at the cost of increased acquisition time. Phase-shifted spectral interferograms may also be acquired simultaneously on separate detectors by employing interferometer topologies, which intrinsically separate phase-shifted signals into different detector channels. Such simultaneous phase-shifted interferometers,

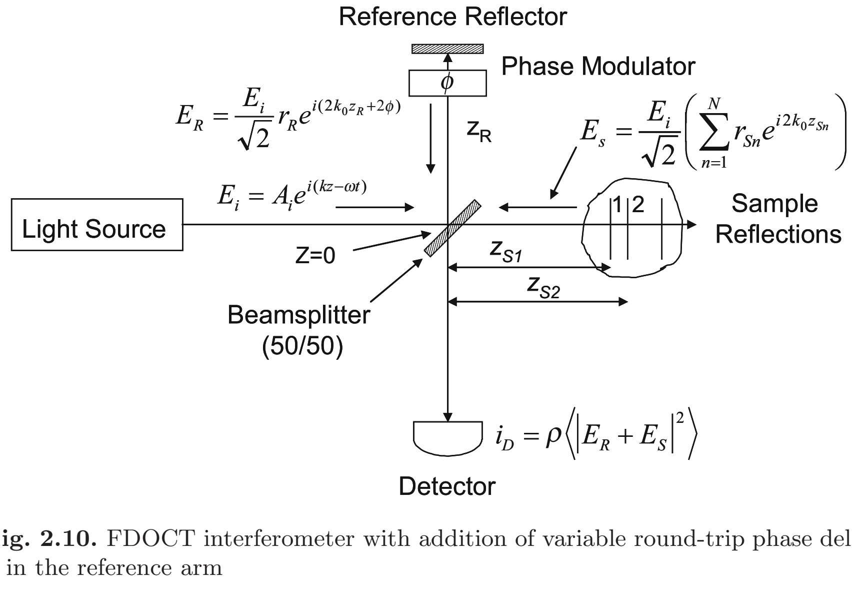

Fig. 2.10. FDOCT interferometer with addition of variable round-trip phase delay ϕ in the reference arm

which use orthogonal polarization states to carry phase-shifted signals, or which employ 3×3 or higher order fiber couplers to separate phase channels, have been constructed. While the analysis to follow assumes that the phase delay is inserted in the reference arm, it is the phase difference between reference and sample arms that matters, thus phase-shifting elements may be placed in either arm.

Rewriting the spectral interferogram from (2.5) with this additional phase delay explicitly included, yields

$$\begin{aligned} I_{\mathrm{D}}(k, 2\phi) = {} & \frac{\rho}{4}\left[S(k)\left[R_{\mathrm{R}} + R_{\mathrm{S1}} + R_{\mathrm{S2}} + \ldots\right]\right] \text{ “DC Terms”} \\ & + \frac{\rho}{2}\left[S(k)\sum_{n=1}^{N}\sqrt{R_{\mathrm{R}}R_{\mathrm{S}n}}\left(\cos\left[2k(z_{\mathrm{R}} - z_{\mathrm{S}n}) + 2\phi\right]\right)\right] \\ & \text{“Cross-correlation Terms”} \\ & + \frac{\rho}{4}\left[S(k)\sum_{n \neq m = 1}^{N}\sqrt{R_{\mathrm{S}n}R_{\mathrm{S}m}}\cos\left[2k(z_{\mathrm{S}n} - z_{\mathrm{S}m}\right]\right] \\ & \text{“Auto-correlation Terms”}. \end{aligned} \tag{2.16}$$

Stepped Phase Shifting Interferometry Approach

If a spectral interferogram with round-trip phase delay $2\phi = \pi$ is acquired and subtracted from a spectral interferogram acquired with no phase delay, then it follows from (2.16) that the DC and autocorrelation terms will be eliminated and the cross-correlation terms doubled:

$$I_{\mathrm{D}}(k, 2\phi = 0) - I_{\mathrm{D}}(k, 2\phi = \pi) = \rho\left[S(k)\sum_{n=1}^{N}\sqrt{R_{\mathrm{R}}R_{\mathrm{S}n}}(\cos[2k(z_{\mathrm{R}} - z_{\mathrm{S}n})])\right]. \tag{2.17}$$

The reversal of the sign of the cosine that gives rise to this result clearly depends only upon the $2\phi = \pi$ phase difference between the spectral interferograms and not upon any arbitrary phase offset to both of them; thus it is important for this and all the following results in this section that the phase-shifted interferograms be acquired either simultaneously, or else quickly, compared to any substantial phase drifting time in the interferometer. The A-scan that results from the inverse Fourier transform of (2.17) also contains only cross-correlation terms; thus the DC and autocorrelation artifacts (but not the complex conjugate artifact) may be eliminated using this 2-step algorithm:

$$\begin{aligned} i_{\mathrm{D}}(z, 2\phi = 0) - i_{\mathrm{D}}(z, 2\phi = \pi) = {} & \frac{\rho}{2}\sum_{n=1}^{N}\sqrt{R_{\mathrm{R}}R_{\mathrm{S}n}}\left[\gamma[2(z_{\mathrm{R}} - z_{\mathrm{S}n})]\right. \\ & \left. + \gamma[-2(z_{\mathrm{R}} - z_{\mathrm{S}n})]\right]. \end{aligned} \tag{2.18}$$

To remove the complex conjugate artifact, at least two spectral interferograms with noncomplementary phase delays (i.e., with 2ϕ different from π radians) must be acquired. For example, if a spectral interferogram with round-trip phase delay $2\phi = 3\pi/2$ is subtracted from a spectral interferogram acquired with round-trip phase delay $2\phi = \pi/2$, the result is a spectral interferogram containing only cross-correlation terms, which is in phase quadrature with the previous result:

$$\begin{aligned} &I_{\mathrm{D}}(k, 2\phi = 3\pi/2) - I_{\mathrm{D}}(k, 2\phi = \pi/2) \\ &\quad = \rho \left[S(k) \sum_{n=1}^{N} \sqrt{R_{\mathrm{R}} R_{\mathrm{S}n}} \left(-\sin\left[2k(z_{\mathrm{R}} - z_{\mathrm{S}n})\right] \right) \right]. \end{aligned} \tag{2.19}$$

Combining all four phase-shifted interferograms yields the result

$$\begin{aligned} &I_{\mathrm{D}}(k, 2\phi = 0) - I_{\mathrm{D}}(k, 2\phi = \pi) + j\left[I_{\mathrm{D}}(k, 2\phi = \pi/2) - I_{\mathrm{D}}(k, 2\phi = 3\pi/2)\right] \\ &\quad = \rho \left[S(k) \sum_{n=1}^{N} \sqrt{R_{\mathrm{R}} R_{\mathrm{S}n}} \left(\cos\left[2k(z_{\mathrm{R}} - z_{\mathrm{S}n})\right] - j \sin\left[2k(z_{\mathrm{R}} - z_{\mathrm{S}n})\right] \right) \right]. \end{aligned} \tag{2.20}$$

This 4-step combination of phase-shifted spectral interferograms inverse transforms to an A-scan free of DC, autocorrelation, and complex conjugate artifacts:

$$\begin{aligned} &i_{\mathrm{D}}(z, 2\phi = 0) - i_{\mathrm{D}}(z, 2\phi = \pi) + j\left[i_{\mathrm{D}}(z, 2\phi = \pi/2) - i_{\mathrm{D}}(z, 2\phi = 3\pi/2)\right] \\ &\quad = \rho \sum_{n=1}^{N} \sqrt{R_{\mathrm{R}}} R_{\mathrm{S}n} \left[\gamma[2(z_{\mathrm{R}} - z_{\mathrm{S}n})] + \gamma[-2(z_{\mathrm{R}} - z_{\mathrm{S}n})] \right. \\ &\qquad \left. + \gamma[2(z_{\mathrm{R}} - z_{\mathrm{S}n})] - \gamma[-2(z_{\mathrm{R}} - z_{\mathrm{S}n})]\right] \\ &\quad = \rho \sum_{n=1}^{N} \sqrt{R_{\mathrm{R}} R_{\mathrm{S}n}} \gamma[2(z_{\mathrm{R}} - z_{\mathrm{S}n})]. \end{aligned} \tag{2.21}$$

It should be noted that if the DC and autocorrelation artifacts are removed through some independent means, i.e., by subtracting pre-acquired averaged spectral interferogram data as described above, then only two phase steps separated by $2\phi = \pi/2$ are required, i.e.,

$$i_{\mathrm{D}}(z, 2\phi = 0) + j\left[i_{\mathrm{D}}(z, 2\phi = \pi/2)\right] = \rho \sum_{n=1}^{N} \sqrt{R_{\mathrm{R}} R_{\mathrm{S}n}} \gamma[2(z_{\mathrm{R}} - z_{\mathrm{S}n})] \tag{2.22}$$

is also true if the component A-scans contain only cross-correlation terms.

Quadrature Projection Phase Correction

In many practical implementations, the phase shifts imposed through external means may not be achievable exactly or may be achromatic. For example, the phase shift imposed on reference arm light by physical modulation of the reference arm delay by, for example, a piezo-electric modulator, depends upon wavenumber. In this case, an additional signal processing step may be introduced to ensure that the supposedly orthogonal signal components are in fact exactly orthogonal, independent of wavenumber. Sarunic has introduced a technique termed quatradure projection phase correction for complex conjugate resolution in FDOCT, which achieves this goal by simply taking the projection of phase-separated signal components upon orthogonal basis vectors [40]. For the example of the simplest two-phase techniques described in the last section, this procedure proceeds as follows.

First, the inverse Fourier transforms of the ostensibly real and imaginary phase-separated signal vectors are separately computed, creating intermediary complex functions A and B:

$$\begin{array}{l} A = \mathrm{I.F.T}\left[-E_1 + E_2 + E_3 - E_4\right] \\ B = \mathrm{I.F.T}\left[-E_1 + E_2 - E_3 + E_4\right] \end{array}. \tag{2.23}$$

Second, the vectors A and B are rotated to lie exactly on the real and imaginary axes. This is done by zeroing out the phase of vector A and subtracting the phase of vector A from that of vector B:

$$\begin{array}{l} A' = |A| \\ B' = |B|\ \mathrm{e}^{\angle B - \angle A} \end{array}. \tag{2.24}$$

Finally, the completely complex conjugate resolved output is computed from the following combination of A' and B':

$$\mathrm{Output} = \mathrm{Im}\left[\mathrm{Re}(A') + j\mathrm{Im}(B')\right]. \tag{2.25}$$

2.7 Sensitivity and Dynamic Range in OCT Systems

One of the advantages of OCT among biophotonic sensing techniques is that, since it borrows so heavily from optical communication technologies, well-developed and inexpensive methodologies for signal optimization are available to approach the quantum detection limit of a single reflected photon. Sensitivity, signal-to-noise ratio (SNR), and dynamic range are often used interchangeably in OCT literature to denote the minimum detectable reflected optical power compared to a perfect reflector, usually expressed in decibel units. Here, we concur with the first two definitions but reserve dynamic range to refer to the range of optical reflectivities observable within a single acquisition or image.

2.7.1 SNR Analysis for Time-Domain OCT

The signal-to-noise ratio for any system is defined as the signal power divided by the noise process variance. We follow the historical development of SNR analysis in OCT by first deriving expressions for TDOCT, then extending the analysis to FDOCT. SNR analysis in TDOCT followed directly from its predecessor technique of optical low-coherence domain reflectometry [41]. To simplify the analysis, we consider only a single sample reflector at position z_{S} and neglect autocorrelation terms. In this case, we can write the total detected photocurrent in a TDOCT system from (2.12) as

$$I_{\mathrm{D}}(z_{\mathrm{R}}) = \frac{\rho S_{\mathrm{TDOCT}}}{2}\left[R_{\mathrm{R}} + R_{\mathrm{S}} + 2\sqrt{R_{\mathrm{R}}R_{\mathrm{S}}}\,\mathrm{e}^{-(z_{\mathrm{R}}-z_{\mathrm{S}})^2\Delta k^2}\,\cos\left[2k_0(z_{\mathrm{R}}-z_{\mathrm{S}})\right]\right]. \tag{2.26}$$

Here, $S_{\mathrm{TDOCT}} = \frac{S_0}{2}$ is the instantaneous source power incident in the sample and reference arms, and is thus the quantity limited by ocular or skin maximum permissible exposure and other safety considerations. The desired OCT signal resides in the third term, whose mean-square peak signal power occurs at $z_{\mathrm{R}} = z_{\mathrm{S}}$ and is given by $\langle I_{\mathrm{D}}\rangle^2_{\mathrm{TDOCT}} = \frac{\rho^2 S_{\mathrm{TDOCT}}{}^2}{2}\left[R_{\mathrm{R}}R_{\mathrm{S}}\right]$. Complete SNR analysis for OCT systems requires consideration of many possible noise sources in addition to shot noise (i.e., bandlimited quantum noise), which is the fundamental limiting noise process for optical detection. The contributions of these noise sources to OCT system performance including design approaches for obtaining shot noise-limited operation have been described in detail for both TDOCT and FDOCT systems. Here we derive expressions for shot noise limited performance. Shot noise variance in an optical receiver is given by $\sigma^2_{\mathrm{sh}} = 2e\bar{I}B$, where e is the electronic charge, $\bar{I}$ is the mean detector photocurrent, and B is the electronic detection bandwidth. In a TDOCT system whose reference arm scans over a depth range $z_{\max}$ during an A-scan acquisition time Δt with velocity $v_{\mathrm{ref}} = z_{\max}/\Delta t$, the reference light frequency is Doppler shifted by $f_{\mathrm{D}} = 2v_{\mathrm{ref}}/\lambda_0 = k_0 z_{\max}/(\pi\Delta t)$, and the resulting FWHM signal power bandwidth is $\Delta f_{\mathrm{D}} = \Delta k_{\mathrm{FWHM}} z_{\max}/(\pi\Delta t)$ (in Hz). The optimal detection bandwidth is approximately twice this value, or $B_{\mathrm{TDOCT}} \approx 2\Delta k_{\mathrm{FWHM}} z_{\max}/(\pi\Delta t)$ [41]. Assuming the light intensity backscattered from the sample is much smaller than that reflected from the reference, the mean detector photocurrent is dominated by the reference arm power and thus $\sigma^2_{\mathrm{TDOCT}} = \rho e S_{\mathrm{TDOCT}} R_{\mathrm{R}} B_{\mathrm{TDOCT}}$. The well-known expression for the SNR of a TDOCT system is thus given by

$$\mathrm{SNR}_{\mathrm{TDOCT}} = \frac{\langle I_{\mathrm{D}}\rangle^2_{\mathrm{TDOCT}}}{\sigma^2_{\mathrm{TDOCT}}} = \frac{\rho S_{\mathrm{TDOCT}} R_{\mathrm{S}}}{2eB_{\mathrm{TDOCT}}}. \tag{2.27}$$

This result, that the SNR is proportional to the detector responsivity ρ and to the power returning from the sample ($=S_{\mathrm{TDOCT}}R_{\mathrm{S}}$), but is independent of the reference arm power level, is reasonable. Note that the detection bandwidth must be increased to accommodate either increased image depth for a given resolution or increased resolution for a given scan depth for a given A-scan acquisition time; thus these modifications are penalized in TDOCT.

2.7.2 SNR Analysis for Fourier-Domain OCT

The first indication that the techniques of Fourier-domain OCT may provide a significant SNR advantage over TDOCT was apparently published by Hausler et al. in 1997 [42]. The analysis was not experimentally confirmed, and as a conference proceedings paper was not widely available. It was not until late 2003 that the publication of three papers in quick succession by independent groups confirmed the advantage both theoretically and experimentally in the case of spectrometer-based FDOCT or SDOCT [10–12]. One of these papers was also the first to recognize the inherent connection between swept-source and spectrometer-based systems, and to demonstrate the identical advantage both theoretically and experimentally for both implementations [11].

To obtain comparable expressions to that of (2.27) for SSOCT and SDOCT systems, we must understand how both signal and noise propagate through the spectral sampling and inverse Fourier transform processes. Under the same assumptions of a single sample reflector and no autocorrelation terms, the sampled version of the spectral interferogram in FDOCT systems (from (2.16)) is

$$I_{\mathrm{D}}[k_m] = \frac{\rho}{2} S_{\mathrm{FDOCT}}[k_m] \left[R_{\mathrm{R}} + R_{\mathrm{S}} + 2\sqrt{R_{\mathrm{R}} R_{\mathrm{S}}} \cos\left[2k_m(z_{\mathrm{R}} - z_{\mathrm{S}})\right] \right]. \quad (2.28)$$

Here, $S_{\mathrm{FDOCT}}[k_m] = \frac{S(k)|_{k=k_m}}{2}$ is that portion of the instantaneous power incident on the sample that corresponds to spectral channel m of the detection system, whether time-multiplexed in SSOCT or on separate detectors in SDOCT. In the discrete case, the inverse Fourier transform operation is implemented as an inverse discrete Fourier transform:

$$i_{\mathrm{D}}[z_m] = \sum_{m=1}^{M} I_{\mathrm{D}}[k_m]\, \mathrm{e}^{+\mathrm{i}k_m z_m/M}. \quad (2.29)$$

Again for the special case of a single sample reflector located at depth $z_{\mathrm{R}} = z_{\mathrm{S}}$, the peak value of the interferometric term in (2.28) inserted into (2.29) is

$$\begin{aligned} i_{\mathrm{D}}[z_m = (z_{\mathrm{R}} - z_{\mathrm{S}}) = 0] &= \frac{\rho}{2}\sqrt{R_{\mathrm{R}} R_{\mathrm{S}}} \sum_{m=1}^{M} S_{\mathrm{FDOCT}}[k_m] \\ &= \frac{\rho}{2}\sqrt{R_{\mathrm{R}} R_{\mathrm{S}}} S_{\mathrm{FDOCT}}[k_m] M; \quad (2.30) \end{aligned}$$

the latter expression under the assumption that each spectral channel has equal power in it (i.e., for a rectangular shaped source spectrum). For a more realistic Gaussian-shaped source spectrum centered at pixel $M/2$ and clipped at its $1/e^2$ points, i.e., $S_{\mathrm{FDOCT}}[k_m] = S_{\mathrm{FDOCT}}[k_{M/2}] \exp[-2(k_m - k_{M/2})^2/(k_{M/2})^2]$, the last factor is $\sum_{m=1}^{M} S_{\mathrm{FDOCT}}[k_{M/2}] = S_{\mathrm{FDOCT}}[k_{M/2}] \cdot M \cdot 0.598$. The interpretation of (2.30) is that the cosinusoidal spectral interference pattern in each separate detection channel from a single reflector adds coherently to give a peak signal power much greater than the signal power in each channel alone. Each detection channel in FDOCT senses interference over a much longer coherence length than the single detection channel in TDOCT, due to its restricted spectral extent. This coherent addition of signal power in FDOCT is not isolated to the trivial choice of $z_m = (z_{\mathrm{R}} - z_{\mathrm{S}}) = 0$ in (2.30); any other choice of $z_m = (z_{\mathrm{R}} - z_{\mathrm{S}})$ would give rise to phase factors in the Fourier kernel, which would still coherently sum to an equivalent combined signal peak. The mean-square peak signal power in FDOCT is thus $\langle i_{\mathrm{D}}\rangle^2_{\mathrm{FDOCT}} = \frac{\rho^2 S^2_{\mathrm{FDOCT}}[k_m]}{4}[R_{\mathrm{R}} R_{\mathrm{S}}]M^2$.

To complete the calculation of the SNR of FDOCT, we must address the issue of how noise transforms from the k-domain to the z-domain. $I_{\mathrm{D}}[k_m]$ can be generalized to include an additive, uncorrelated Gaussian white noise term $\alpha[k_m]$. $\alpha[k_m]$ has a mean of zero, a standard deviation $\sigma[k_m]$, and a lower limit set by shot noise. Again assuming $R_{\mathrm{R}} >> R_{\mathrm{S}}$, in the shot noise limit, $\sigma^2_{\mathrm{FDOCT}}[k_m] = e\rho S_{\mathrm{FDOCT}}[k_m] R_{\mathrm{R}} B_{\mathrm{FDOCT}}$. In this case, however, the noise in each spectral channel is uncorrelated; thus the noise variances add incoherently in the inverse discrete Fourier summation to give $\sigma^2_{\mathrm{FDOCT}}[z_m] = \sum_{m=1}^{M} \sigma^2_{\mathrm{FDOCT}}[k_m] = e\rho S_{\mathrm{FDOCT}}[k_m] R_{\mathrm{R}} B_{\mathrm{FDOCT}} M$. Thus, the SNR of FDOCT in general is given by

$$SNR_{\mathrm{FDOCT}} = \frac{\langle i_{\mathrm{D}}\rangle^2_{\mathrm{FDOCT}}}{\sigma^2_{\mathrm{FDOCT}}} = \frac{\rho S_{\mathrm{FDOCT}}[k_m] R_{\mathrm{S}}}{4eB_{\mathrm{FDOCT}}} M. \tag{2.31}$$

To specialize this general expression for SDOCT and SSOCT specifically and to compare the resulting sensitivities to that of TDOCT, we assume an identical A-scan length $z_{\max}$ and acquisition time Δt for all three systems, and that the instantaneous sample arm power (which is limited by safety or source availability considerations in practice) is the same. We also assume a source with rectangular-shaped spectrum, at least initially. A summary of the results of this section is provided in Table 2.2. For an SSOCT system, the allowable sample illumination power for each spectral channel is the same as the total illumination power in TDOCT, since only one channel is illuminated at a time. Thus, $S_{\mathrm{SSOCT}}[k_m] = S_{\mathrm{TDOCT}}$. The detection bandwidth in SSOCT is limited by the analog-to-digital sampling frequency $f_{\mathrm{s}} = M/\Delta t = 1/(2\pi)4z_{\max}\Delta k/\Delta t = 2\Delta k z_{\max}/(\pi\Delta t)$, where (2.22) relates $z_{\max}$ to $\delta_{\mathrm{s}}k$ and $\Delta k = M\delta_{\mathrm{s}}k$ is the entire range of wavenumbers scanned. Assuming a scanning range of $\Delta k = 2k_{\mathrm{FWHM}}$ is chosen and that an anti-aliasing filter is used to limit the detection bandwidth to $B_{\mathrm{SSOCT}} = f_{\mathrm{s}}/2$, then $B_{\mathrm{SSOCT}} = B_{\mathrm{TDOCT}}$. For an SDOCT system, where all spectral channels are illuminated and detected simultaneously, the allowable power per spectral channel is decreased by the factor M, i.e., $S_{\mathrm{SDOCT}}[k_m] = S_{\mathrm{TDOCT}}/M$. Also the SDOCT detection bandwidth $B_{\mathrm{SDOCT}} = B_{\mathrm{TDOCT}}/M$, since the signals from each channel are integrated over the entire A-scan time. Thus, we can

Table 2.2. Shot-noise limited SNR expressions for time-domain (TDOCT), spectral-domain (SDOCT), and swept-source OCT (SSOCT), normalized to the sample arm instantaneous power S_{TDOCT} and detection bandwidth B_{TDOCT} used in TDOCT

	Time-Domain OCT (TDOCT)	Swept-Source OCT (SSOCT)	Spectral-Domain OCT (SDOCT)
Mean-square peak signal power $\langle I_{\mathrm{D}}\rangle^2$	$\frac{\rho^2 {S_{\mathrm{TDOCT}}}^2}{2}\,[R_{\mathrm{R}} R_{\mathrm{S}}]$	$\frac{\rho^2 S_{\mathrm{TDOCT}}^2}{4}\,[R_{\mathrm{R}} R_{\mathrm{S}}]\,M^2$	$\frac{\rho^2 S_{\mathrm{TDOCT}}^2}{4}\,[R_{\mathrm{R}} R_{\mathrm{S}}]$
Noise variance σ^2	$\rho e S_{\mathrm{TDOCT}} R_{\mathrm{R}} B_{\mathrm{TDOCT}}$	$e\rho S_{\mathrm{TDOCT}} R_{\mathrm{R}} B_{\mathrm{TDOCT}} M$	$\frac{e\rho S_{\mathrm{FDOCT}}[k_m] R_{\mathrm{R}} B_{\mathrm{FDOCT}}}{M}$
Signal-to-noise ratio $\mathrm{SNR} = \frac{\langle I_{\mathrm{D}}\rangle^2}{\sigma^2}$	$\frac{\rho S_{\mathrm{TDOCT}} R_{\mathrm{S}}}{2eB_{\mathrm{TDOCT}}}$	$\frac{\rho S_{\mathrm{TDOCT}} R_{\mathrm{S}}}{2eB_{\mathrm{TDOCT}}}\frac{M}{2}$	$\frac{\rho S_{\mathrm{TDOCT}} R_{\mathrm{S}}}{2eB_{\mathrm{TDOCT}}}\frac{M}{2}$

write expressions for the SNR of both SSOCT and SDOCT systems compared to TDOCT:

$$\mathrm{SNR}_{\mathrm{SDOCT}} = \mathrm{SNR}_{\mathrm{SSOCT}} = \frac{\rho S_{\mathrm{TDOCT}} R_{\mathrm{S}}}{4eB_{\mathrm{TDOCT}}} M = \mathrm{SNR}_{\mathrm{TDOCT}} \frac{M}{2}. \qquad (2.32)$$

The factor of $M/2$ improvement in both SSOCT and SDOCT over TDOCT can be simply understood from the fact that both FDOCT methods sample all depths all the time, giving rise to a potential SNR improvement by a factor M; however, both FDOCT methods generate redundant data for positive and negative sample displacements relative to the reference position, decreasing the SNR improvement by a factor of 2 [11]. The factor of M in (2.32) also depends upon the assumption of the source having equal power in all spectral channels, which is unrealistic and would lead to undesirable ringing in the inverse transformed data in any case. More realistic spectral shapes, such as the Gaussian shape discussed earlier, would decrease the SNR by an additional factor of about 2. It is clear, however, that filling the spectral channels with as much power as possible translates directly into increased SNR. Taking these factors into account and assuming that $M \approx 10^3$ for a realistic swept-source laser or detector array, we conclude that FDOCT systems are theoretically capable of up to 20 dB greater sensitivity than TDOCT systems.

It is also important to note that the theoretical SNR gain of SDOCT and SSOCT compared to TDOCT derived above rests upon the assumption of shot noise-limited detection in each detection channel. As has been addressed in earlier publications for the case of TDOCT, achievement of this limit requires sufficient reference arm power to assure shot noise dominance, but usually requires significant reference arm attenuation to minimize excess noise. In the case of SSOCT, the SNR of the spectral domain interferometric signal output by the photodetector is equal to the SNR of a time-domain OCT system photodetector output operating at the same line rate and reference arm power; thus the optimal reference arm power level for SSOCT is expected to be similar to that for TDOCT. In SDOCT, where the reference arm power is dispersed onto M photodetectors, the total reference power required to achieve shot noise-limited detection on all receivers simultaneously is more than that required for SSOCT and TDOCT by a factor of M. However, whether or not this requires redesign of the interferometer coupling ratio depends upon the desired A-scan rate and the noise performance of the detectors used.

Acknowledgments

We gratefully acknowledge the contributions of past and present graduate students and post-doctoral members of the Izatt Biophotonics Laboratory at Duke University, particularly Brian Applegate, Brad Bower, Anjul Davis, Marinko Sarunic, and Changhuei Yang. We also acknowledge a fruitful discussion with Prof. Min Gu. Portions of this work were supported by NIH grants EY013516, RR019769, EY017393, and EB006338, NSF grant BES-0216403, and the Whitaker Foundation.

References

1. J.M. Schmitt et al., Phys. Med. Biol. **39**(10), 1705 (1994)
2. J.A. Izatt et al., Opt. Lett. **19**(8), 590 (1994)
3. Y. Pan et al., Appl. Opt. **34**, 6564 (1995)
4. J.A. Izatt et al., IEEE J. Sel. Top. Quant. Electron. **2**(4), 1017 (1996)
5. J.M. Schmitt, A. Knuttel, J. Opt. Soc. Am. A Opt. Image Sci. Vis. **14**(6), 1231 (1997)
6. L.S. Dolin, Radiophys. Quant. Electron. **41**(10), 850 (1998)
7. A.G. Podoleanu, D.A. Jackson, Appl. Opt. **38**(10), 2116 (1999)
8. A.M. Rollins, J.A. Izatt, Opt. Lett. **24**(21), 1484 (1999)
9. A.G. Podoleanu, Appl. Opt. **39**(1), 173 (2000)
10. R. Leitgeb, C.K. Hitzenberger, A.F. Fercher, Opt. Exp. **11**(8), 889 (2003)
11. M.A. Choma et al., Opt. Exp. **11**(18), 2183 (2003)
12. J.F. de Boer et al., Opt. Lett. **28**(21), 2067 (2003)
13. A.F. Fercher, J. Biomed. Opt. **1**(2), 157 (1996)
14. J.M. Schmitt, IEEE J. Sel. Top. Quant. Electron. **5**(4), 1205 (1999)
15. M.R. Hee, in *Handbook of Optical Coherence Tomography*, ed. by B.E. Bouma, G.J. Tearney (Marcel Dekker, New York, 2002), pp. 41–66
16. M.E. Brezinski, in *Optical Coherence Tomography Principles and Applications* (Academic Press, New York, 2006), pp. 97–146
17. T. Wilson, *Confocal Microscopy* (Academic Press, London, 1990)
18. M. Gu, C. Sheppard, X. Gan, J. Opt. Soc. Am. B **8**, 1755 (1991)
19. M. Gu, *Principles of Three-Dimensional Imaging in Confocal Microscopes* (World Scientific, Singapore, 1996)
20. J.M. Schmitt, S.L. Lee, K.M. Yung, Opt. Commun. **142**, 203 (1997)
21. S.-W. Huang et al., Opt. Exp. **15**(10), 6210 (2007)
22. A.F. Fercher et al., Opt. Commun. **117**(1–2), 43 (1995)
23. G. Hausler, M.W. Lindner, J. Biomed. Opt. **3**(1), 21 (1998)
24. M. Wojtkowski et al., J. Biomed. Opt. **7**(3), 457 (2002)
25. S.R. Chinn, E.A. Swanson, J.G. Fujimoto, Opt. Lett. **22**(5), 340 (1997)
26. B. Golubovic et al., Opt. Lett. **22**(22), 1704 (1997)
27. F. Lexer et al., Appl. Opt. OT **36**(25), 6548 (1997)
28. U.H.P. Haberland, V. Blazek, H.J. Schmitt, J. Biomed. Opt. **3**(3), 259 (1998)
29. M. Wojtkowski et al., Opt. Lett. **27**(16), 1415 (2002)
30. R.A. Leitgeb et al., Opt. Lett. **28**(22), 2201 (2003)
31. M.A. Choma, C. Yang, J.A. Izatt, Opt. Lett. **28**(22), 2162 (2003)
32. S.H. Yun et al., Opt. Exp. **12**, 4822 (2004)
33. E. Gotzinger et al., Opt. Exp. **13**(2), 583 (2005)
34. M.V. Sarunic et al., Opt. Exp. **13**, 957 (2005)
35. A.M. Davis, M.A. Choma, J.A. Izatt, J. Biomed. Opt. **10**(6), 064005 (2005)
36. J. Zhang, J.S. Nelson, Z.P. Chen, Opt. Lett. **30**(2), 147 (2005)
37. S.H. Yun et al., Opt. Exp. **11**(26), 3598 (2003)
38. B. Bhushan, J.C. Wyant, C.L. Koliopoulos, Appl. Opt. **24**, 1489 (1985)
39. A. Dubois, J. Opt. Soc. Am. A. **18**, 1972 (2001)
40. M.V. Sarunic, B.E. Applegate, J.A. Izatt, Opt. Lett. **31**(16), 2426 (2006)
41. E.A. Swanson et al., Opt. Lett. **17**(2), 151 (1992)
42. M. Bail et al., *Optical Coherence Tomography by Spectral Radar for the Analysis of Human Skin* (SPIE, US, 1997)

Springer

http://www.springer.com/978-3-540-77549-2

Optical Coherence Tomography
Technology and Applications
(Eds.)W. Drexler; J.G. Fujimoto
2008, XXX, 1346 p. 758 illus., 287 in color. In 2 volumes,
not available separately., Hardcover
ISBN: 978-3-540-77549-2